# Can high-temperature, high-heat flux hydrothermal vent fields be explained by thermal convection in the lower crust along fast-spreading Mid-Ocean Ridges?

Fabrice J Fontaine, M. Rabinowicz, M. Cannat

## RESEARCH ARTICLE

**Key Points:**
- The gabbroic magma chamber in the lower crust along the axis of fast MOR can convect as a viscous fluid
- Magmatic convection controls the distribution of hydrothermal fields and the pattern of melt delivery in the AML along fast MOR
- Lower crust convection offers new perspectives on the formation of the lower crust of fast MOR

**Correspondence to:**
F. J. Fontaine,
fontaine@ipgp.fr

# Can high-temperature, high-heat flux hydrothermal vent fields be explained by thermal convection in the lower crust along fast-spreading Mid-Ocean Ridges?

**Fabrice J. Fontaine[1,2], M. Rabinowicz[3], and M. Cannat[1]**

[1]Institut de Physique du Globe de Paris, UMR CNRS 7154, Paris, France, [2]Now at Observatoire du Piton de la Fournaise, La Réunion Island, [3]Laboratoire GET, UMR CNRS 5563, Toulouse, France

**Abstract** We present numerical models to explore possible couplings along the axis of fast-spreading ridges, between hydrothermal convection in the upper crust and magmatic flow in the lower crust. In an end-member category of models corresponding to effective viscosities $\mu_M$ lower than $10^{13}$ Pa.s in a melt-rich lower crustal along-axis corridor and permeability k not exceeding $\sim 10^{-16}$ m$^2$ in the upper crust, the hot, melt-rich, gabbroic lower crust convects as a viscous fluid, with convection rolls parallel to the ridge axis. In these models, we show that the magmatic-hydrothermal interface settles at realistic depths for fast ridges, i.e., 1–2 km below seafloor. Convection cells in both horizons are strongly coupled and kilometer-wide hydrothermal upflows/plumes, spaced by 8–10 km, arise on top of the magmatic upflows. Such magmatic-hydrothermal convective couplings may explain the distribution of vent fields along the East (EPR) and South-East Pacific Rise (SEPR). The lower crustal plumes deliver melt locally at the top of the magmatic horizon possibly explaining the observed distribution of melt-rich regions/pockets in the axial melt lenses of EPR and SEPR. Crystallization of this melt provides the necessary latent heat to sustain permanent $\sim 100$ MW vents fields. Our models also contribute to current discussions on how the lower crust forms at fast ridges: they provide a possible mechanism for focused transport of melt-rich crystal mushes from moho level to the axial melt lens where they further crystallize, feed eruptions, and are transported both along and off-axis to produce the lower crust.

## 1. Introduction

The thermal regime of oceanic-spreading centers is strongly dependent on the heat and mass fluxes between an upper crustal horizon that is affected by hydrothermal circulation, and the underlying magmatic complex. These fluxes are key processes controlling, crustal cooling, crystallization and accretion, eruptions and hydrothermal flow dynamics. Figure 1a, drawn after *Carbotte et al.* [2013], is a sketch of the principal lithological units at the axis of fast mid-ocean ridges. The brittle, "hydrothermal" upper crust is mostly composed of solidified dykes and pillows and is underlain by a ductile, magmatic lower crust composed of an Axial Melt Lens (AML), associated to secondary AMLs (SAMLs) below, all located above a region of low seismic velocities (LVZ: Low velocity Zone) that is interpreted as a crystal-rich mush zone [*Detrick et al.*, 1993; *Dunn et al.*, 2000; *Marjanović et al.*, 2014]. In the lower part of this crustal LVZ, seismic studies have evidenced the presence of melt-rich sills/lens at [*Garmany*, 1989; *Crawford et al.*, 1999; *Nedimović et al.*, 2005] and above the moho transition zone [*Singh et al.*, 2006; *Canales et al.*, 2009]. The AML is continuous along-axis, and is 0.5–1 km wide across-axis. The Axial Summit Trough (AST) where most eruptions are documented to occur is also continuous along axis and < 0.5 km-wide across-axis [*Fornari et al.*, 1998]. The gabbroic "magma chamber" underneath is narrow, and only 4–6 km-wide in the across-axis direction and has steep-sided walls [*Dunn et al.*, 2000]. The vertical distribution of maximum melt to crystal proportions in this axial magma chamber, as derived from analyses of seismic velocity variations at the fast-spreading EPR, is not uniform and varies between 10–38% at 2 km-depth and 3–11% at 6 km, depending on the size and shape assumed for the melt-filled porosity [*Dunn et al.*, 2000].

Although the magmatic and hydrothermal layers are strongly coupled by nature, historically, studies of their thermal regime have followed separate paths. In most studies of mid-ocean ridge hydrothermal convection, the heat provided by magma advection, magma crystallization, and latent heat release, and by simple
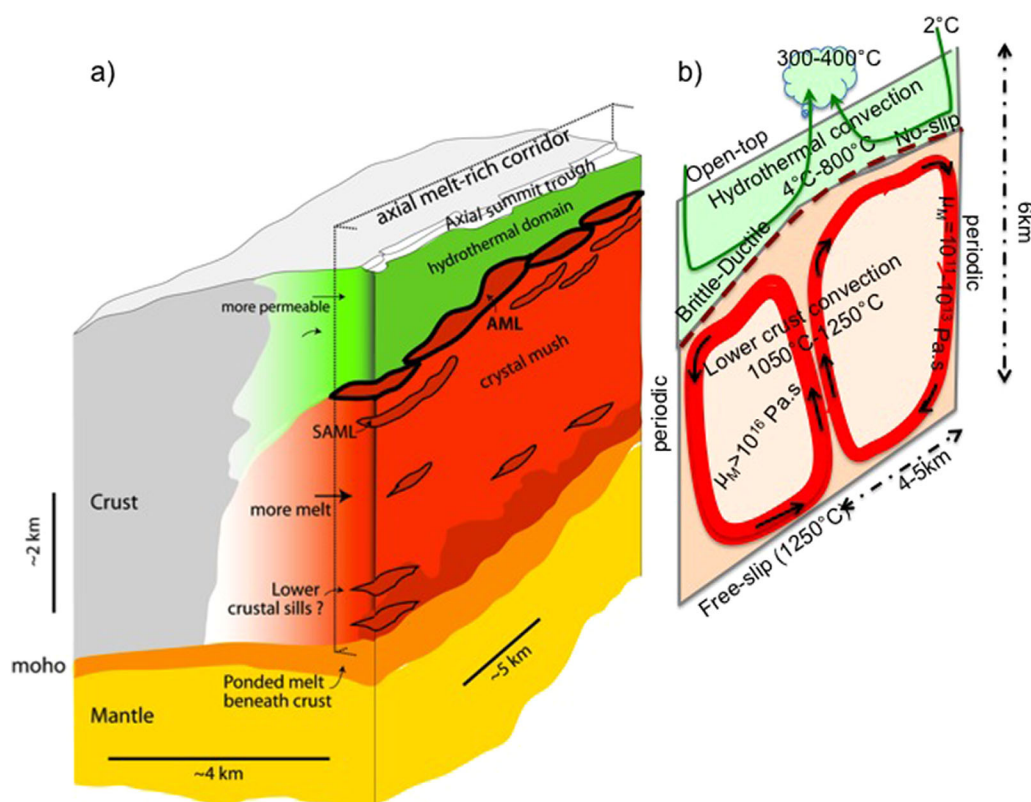
**Figure 1.** (a) Cartoon illustrating the structure of the axial crustal domain, from seafloor to moho at fast-spreading ridges (modified after *Carbotte et al.* [2013]). (b) Simplified 2-D, along-axis model geometry.

conduction, is not explicitly considered and an ad hoc temperature or heat flux is prescribed at the base of the hydrothermal horizon [e.g., *Coumou et al.*, 2006; *Fontaine and Wilcock*, 2007]. Conversely, thermal models of the lower crust usually incorporate hydrothermal cooling in the upper crust by artificially increasing the conductivity of this horizon by a factor Nu—the Nusselt number—characterizing the vigor of hydrothermal convection [e.g., *Morgan and Chen*, 1993]. These approaches preclude a precise description of the thermal state of the crust at mid-ocean ridges.

A few studies have attempted to address the question of the thermal regime of the coupled system composed by (i) the ductile, magmatic lower crust, and (ii) the hydrothermal, brittle upper crust. Because of the conceptual, theoretical, and numerical challenges of coupling magmatic and hydrothermal processes, these studies are restricted to two-dimensional geometries, along the across-axis dimension as in *Cherkaoui et al.* [2003] and *Theissen-Krah et al.* [2011, 2016] where hydrothermal, cellular-type, flow dynamics is coupled to crustal accretion.

*Cherkaoui et al.* [2003] use a steady state approach in which new lithosphere accretes continuously and is advected horizontally with spreading velocity. They model cellular hydrothermal circulation in the brittle crust using a two-dimensional Darcy-type formalism. They focus on the effects of hydrothermal cooling on the cross-axis thermal structure of the lower crust magmatic layer and highlight the role of permeability on the shape of the magmatic-hydrothermal interface and on the production of off-axis hydrothermal cells. They argue that the steep-sided walls of the magma chamber could be attributed to the cooling effect of deep, off-axis hydrothermal circulation.

*Theissen-Krah et al.* [2011] fully couple transient viscous flow in the lower crust to hydrothermal circulation. They build upon *Morgan and Chen* [1993] keeping their model of crustal accretion but modifying the formalism to solve for 2-D Darcy-type hydrothermal flow rather than simply enhancing the conductivity in the brittle crust. They focus on constraining the depth to the axial melt lens (AML) and the cross-axis shape of the brittle/ductile interface at intermediate-to fast-spreading axes. In particular, they show that the

observed AML depths require a narrow range of permeability, i.e., 3–6 $\times$ $10^{-15}$ m$^2$, lower than the 4 $\times$ $10^{-14}$ m$^2$ found by *Cherkaoui et al*. [2003].

*Theissen-Krah et al*. [2016] propose a refined version of the formalism of *Theissen-Krah et al*. [2011], in which various modes of crustal accretion are possible and test the effects of crystallizing the lower crust either (i) totally in the AML at the top of the gabbroic magma chamber (the "gabbro-glacier model") [e.g., *Morgan and Chen*, 1993] or (ii) only partly in the AML with the rest crystallizing in situ, at any depth between the moho and the top of the gabbro section (the "sheeted-sills model") [e.g., *Kelemen et al*., 1997]. Models matching observations of melt lens depth, thermal structure, and melt fraction always require less than 50% of the lower crust crystallizing in situ.

These models coupling crustal accretion to cellular hydrothermal convection have contributed to improving and refining our knowledge of the axial thermal regime and crustal formation but have the intrinsic basic premise that the lower crust is accreted "passively." However, magma chambers in various geological settings are known to be unstable with regards to thermal convection [e.g., *Brandeis and Jaupart*, 1986]. In the present work, we study this possibility for the gabbroic magma chamber along the axis of fast-spreading ridges. In section 2, we first constrain the key parameter controlling convection in the chamber, i.e., its viscosity. We posit that it could be low enough in a narrow (0.5–1 km-wide) along-axis lower crustal domain, or "corridor," embedded within the low viscosity zone of *Dunn et al*. [2000], where the melt content is on average high and where most AML replenishment, and most eruptions are documented to occur (Figure 1). We then propose an original conceptual model for the thermal regime of the axial domain of fast-spreading ridges. In this conceptual model, the crust can be seen as a continuous, coupled, "two-layer" system where viscous convection transports heat from the moho to the top of the gabbroic section, relayed by hydrothermal convection in the upper brittle/fractured crust, from the base of the dyke section to the seafloor (Figure 1b). In section 3, we study the dynamic modalities of heat and mass transfers in such a thermally coupled two-layer convective system and present two-dimensional numerical simulations of along-axis convective thermal couplings between a fluid-like, viscous magmatic lower layer and a porous-like, hydrothermal upper layer. We use these models to quantify the typical wavelengths of the two convective processes. Finally, in section 4 we discuss our results in the light of geological and geophysical observations at fossil (ophiolites) and fast MOR sites, and place our models in the more general context of oceanic hydrothermal processes and crustal accretion.

## 2. The "Two-Layers," Fluid-Porous/Magmatic-Hydrothermal Conceptual Model

For convection to arise in a fluid-like layer, its Rayleigh number must exceed a critical value. We call Ra$_M$ the Rayleigh number of the lower crust magma chamber with subscript M referring to it. Ra$_M$ is given by:

$$Ra_M = \rho_M \Delta T_M \alpha_M g (H_M)^3 / \mu_M \kappa \qquad (1)$$

where $\rho_M$, $\alpha_M$, $\mu_M$, and $\kappa$ represent the density, the coefficient of thermal expansion, the effective viscosity, and the thermal diffusivity of the mush, respectively. Parameter values are given in Table 1. Besides, g, H$_M$, and $\Delta T_M$ are the gravity constant, the height, and the bottom to top temperature difference across the mush layer, respectively. We choose H$_M$ = 4500 m, considering that at first-order the whole axial crust is 6000 m-thick and that the upper brittle part is 1500 m-thick, i.e., that the AML is found at a depth of $\sim$1500 m below seafloor (Figure 1). Additional geological arguments are required to constrain $\Delta T_M$. The temperature at the top of the mush, at the transition between the gabbros and the sheeted-dykes complex, is set as $\sim$1050°C, constrained by the liquidus of residual liquid after extensive fractional crystallization [*Sinton and Detrick*, 1992]. The temperature at the bottom of the mush, at the transition zone between the crust and the mantle, is 1250°C and is defined by the liquidus temperature of primitive MORB [*Sinton and Detrick*, 1992].

This lower interface is known from both ophiolite studies [e.g., *Benn et al*., 1988] and seismic experiments at fast-spreading ridges [*Crawford et al*., 1999; *Garmany*, 1989; *Nedimović et al*., 2005] to be rich in melt. This defines a gabbroic mush layer with a top no-slip interface and a bottom free one. Classical, stability-based theoretical arguments indicate that the onset of convection in this layer is possible when Ra$_M$ exceeds the critical value of $\sim$1300 [*McKenzie et al*., 1974]. This condition is reached when the viscosity is $\sim$10$^{16}$ Pa.s.

**Table 1.** Model Parameters and Notations

| Parameters | Names | Equations | Amplitude |
|---|---|---|---|
| X | Horizontal coordinates (m) | | |
| Z | Vertical coordinates (m) | | |
| H | Total system thickness (m) | | $6 \times 10^3$ |
| L | System length (along-axis, m) | | $1.8 \times 10^4$ |
| x′ | Dimensionless horizontal coordinates (m) | x/L | |
| z′ | Dimensionless vertical coordinates (m) | z/H | |
| Δx′ | Dimensionless grid size in x direction | | 1/256 |
| Δz′ | Dimensionless grid size in z direction | | 1/256 |
| $H_M{}^a$ | Magma system thickness (m) | | $4.5 \times 10^3$ |
| $H_H$ | Hydrothermal system thickness (m) | | $1.5 \times 10^3$ |
| $D_H$ | Depth to base of hydrothermal system (m) | | |
| $D_M$ | Depth to top of magmatic system (m) | | |
| d | Gabbroic grain size (m) | | $10^{-3}$–$3 \times 10^{-3}$ [Yoshinobu and Hirth, 2002] |
| $K_H$ | Hydrothermal system permeability (m$^2$) | | |
| $K_M$ | Magma system permeability (m$^2$) | $\dfrac{\phi^3 d^2}{180(1-\phi)^2}$ | $7.1 \times 10^{-12}$ (Φ = 0.1, d = $10^{-3}$) $6.4 \times 10^{-11}$ (Φ = 0.1, d = $3 \times 10^{-3}$) |
| R | Hydraulic resistivity (m/s) | KHρHg/μH | [Meyer et al., 1993; Pitzer et al., 1984; Anderko and Pitzer, 1993] |
| T | Temperature (℃) | | 4–1250 |
| $T_{cut}$ | Hydrothermal system basal temperature (℃) | | 800 |
| $T_{melt}$ | Magma system top temperature (℃) | | 1050 |
| P | Pressure (Pa) | | |
| $V_M$ ($U_M, W_M$) | Magmatic velocity vector (m/s) | | |
| $V_H$ ($U_H, W_H$) | Hydrothermal velocity vector (m/s) | | |
| t | Time (s) | | |
| $Ra_M$ | Magma system geological Rayleigh number | | |
| $Ra_{M-num}$ | Magma system numerical Rayleigh number | | $10^5$–$10^8$ |
| $Ra_{M-num/eq}$ | Magma system numerical equivalent Rayleigh number | | |
| $Ra_{H-num}$ | Hydrothermal numerical Rayleigh number | | 0–500 |
| $Ra_{H-num/eq}$ | Hydrothermal system numerical equivalent Rayleigh number | | |
| Nu | Nusselt number at the base of the system | | |
| $l_c$ | Compaction length (m) | $\left(\dfrac{K_M \mu_M}{\phi_M \mu_m}\right)^{1/2}$ | 850–2550 |
| θ | Dimensionless temperature | T/ΔT | |
| $\psi_M$ | Magma system stream function (m$^2$/s) | | |
| $\Psi_H$ | Hydrothermal system stream function (m$^2$/s) | | |
| $\alpha_M$ | Magma system thermal expansion (1/°K) | | $6 \times 10^{-5}$ [Brandeis and Jaupart, 1986] |
| $\mu_b{}^b$ | Basaltic melt viscosity (Pa.s) | | 10–100 [Bottinga and Weill, 1972] |
| $\mu_H{}^c$ | Hydrothermal fluid viscosity (Pa.s) | | [Meyer et al., 1993] |
| $\mu_{Hr}$ | Hydrothermal fluid reference viscosity (Pa.s) | | $5 \times 10^{-5}$ [Meyer et al., 1993] |
| $\mu_M$ | Magma system viscosity (Pa.s) | | $10^{11}$–$10^{18}$ |
| κ | System diffusivity (m$^2$/s) | | $10^{-6}$ [Wilson et al., 1988] |
| γ | Ratio of volumetric heat capacities | | $4 \times 10^{-2}$–2 [Pitzer et al., 1984; Anderko and Pitzer, 1993] |
| $\rho_M$ | Magma system density (kg/m$^3$) | | 2900 [Iturrino et al., 1996] |
| $\rho_H$ | Hydrothermal fluid density (kg/m$^3$) | | [Pitzer et al., 1984; Anderko and Pitzer, 1993] |
| Φ | Lower crust melt concentration | | |
| $\Delta T_M$ | Temperature contrast in the mush (℃) | | 200 |
| $\Delta T_H$ | Temperature contrast in the hydrothermal system (℃) | | 796 |
| ΔT | Temperature contrast in the whole system (℃) | | 1246 |
| ΔH | Hydrothermal/magmatic thermal boundary layer (m) | | |
| Δρ | Density contrast between solid gabbros and melt (kg/m$^3$) | | 200–250 [Brandeis and Jaupart, 1986; Iturrino et al., 1996] |
| $\Delta\rho_H$ | Density contrast between hot and cold hydrothermal fluids (kg/m$^3$) | | 900 [Pitzer et al., 1984; Anderko and Pitzer, 1993] |

[a]M refers to the lower crust, two-phase, mush-like (melt + crystallized gabbroic matrix) magmatic system.
[b]b refers to the basaltic melt in the lower crust.
[c]H refers to the hydrothermal system.

Deformation experiments on gabbro samples and petrological data from the Oman ophiolites show that a 10% melt-rich gabbro samples has a viscosity of $10^{18}$ Pa.s [Yoshinobu and Hirth, 2002]. This value, which is two orders of magnitude greater than the one for which the Rayleigh exceeds critical, corresponds to the viscosity of a stationary magma chamber. However, viscosity values more consistent with the critical value of $10^{16}$ Pa.s can be found in the literature when the axial lower crust is seen as a dynamic body. In the accretion models initially developed by Morgan and Chen [1993] and further improved and exploited by Theissen-Krah et al. [2011, 2016], the dynamical viscosity is exactly the critical value of $10^{16}$ Pa.s. In

*Rabinowicz et al.* [1987], the viscosity used for the lower crust and Moho transition zones is about $10^{15}$ Pa.s. This value is chosen in order to achieve mechanical coupling at the asthenosphere-lithosphere boundary to explain geological observations (parallel magmatic lineations and foliations in the crustal and mantle domains above and below the moho, respectively). Based on petrophysical data from the Oman ophiolite, *Nicolas and Ildefonse* [1996] and *Chenevez et al.* [1998] also infer viscosities down to $10^{15}$ Pa.s for the axial gabbroic mush.

Viscosities $\sim 10^{16}$ Pa.s make it possible for convective instabilities to arise within the mush in a weak regime just above critical ($Ra_M < \sim 10^4$). Convective transport of the mushy material will then cause shear. Numerical models of convection in which the fluid viscosity is strain rate-dependent show that the flow concentrates in regions of low-viscosity at the periphery of the convective cells where the strain rate is high, while the regions in the core of the cell have higher viscosity because of lower strain rate [e.g., *Parmentier et al.*, 1976; *Parmentier*, 1978]. Moreover, a drastic increase of melt content can be predicted in the most intensely sheared regions [e.g., *Rabinowicz and Vigneresse*, 2004; *Rabinowicz et al.*, 2010]. *Allwright and Katz* [2014], *Katz and Takei* [2013], and *Takei and Katz* [2013] have shown that melt-solid segregation in pipe Poiseuille flow, which is a good approximation of the flow field in the horizontal and vertical limbs of a convective cell, leads to liquid/melt concentration in zones of larger shear stresses and to its migration from the center of the pipe towards the walls. The mean melt concentration can be increased by a factor of 3–4 near the walls of the pipe. This shear-induced melt-enrichment process can reduce the viscosity of the limbs of the convective cells by several orders of magnitude. Crystal mush viscosity is therefore a dynamic parameter and has the potential to vary by several orders of magnitude in time and space, because of deviatoric stresses and changes in melt concentration [e.g., *Lejeune and Richet*, 1995; *Picard et al.*, 2013]. *Picard et al.* [2013] infer viscosity down to $10^{11}$ Pa.s for mush with 20–25% melt, based on deformation experiments of plagioclase aggregates (plagioclase being the mineral phase that controls the rheology of the gabbroic lower oceanic crust). With such a low viscosity, the maximum Rayleigh number is $Ra_M \sim 3 \times 10^8$, i.e., more than five orders of magnitude greater than the critical one.

The numerical experiments of *Katz and Takei* [2013] for two-phase Poiseuille flow also show that melt concentration toward the border of the mush column influences the balance of forces (gravitational, friction, internal) at the scale of the whole model column: its velocity increases as the melt segregation processes evolve with time, indicating a drastic decrease of the resistance to flow. This acceleration is the dynamical response of the whole two-phase column to the net reduction of its effective viscosity by several orders of magnitude. *Katz and Takei* [2013] show that the timing of this viscosity reduction during the melt segregation process depends critically on the ratio of the compaction length $l_c$ to the system height $H_M$. According to the formalism of *Bercovici et al.* [2001], $l_c$ is given by:

$$l_c = (K_M \mu_M)^{1/2} / (\phi \mu_b)^{-1/2} \tag{2}$$

where $\phi$, $K_M$, and $\mu_b$ designate the porosity, permeability of the mush, and the melt viscosity, respectively (see Table 1 for characteristics values). The numerical experiments in *Katz and Takei* [2013] show that when $l_c \geq H_M \sqrt{\phi}$ ($\sim 4500 \times \sqrt{0.1}$ m $\cong 1400$ m), the viscosity decrease is drastic and of at least one order of magnitude, evolving rapidly with time. Using the typical values summarized in Table 1 for the physical parameters, a melt content $\phi = 10\%$ and $\mu_M = 10^{18}$ Pa.s [i.e., *Yoshinobu and Hirth*, 2002] for the gabbroic mush before compaction, one can see that the condition $l_c \geq H_M \sqrt{\phi}$ is almost always satisfied for the lower crust as $l_c$ ranges from $\sim 850$ m (grain size of 1 mm, and highest basaltic melt viscosity of 100 Pa.s) [e.g., *Bottinga and Weill*, 1972] to $\sim 2550$ m (grain size of 3 mm, and lowest basaltic melt viscosity of 10 Pa.s). This indicates that segregation-induced reduction of the mush effective viscosity is likely to occur in the melt-rich lower crustal axial domain (Figure 1) of fast-spreading ridges.

The conceptual model that we will consider in our numerical models is shown in Figure 1b. Along the ridge axis, the lower crust is a mush composed of basaltic melt and partly crystallized gabbros. Where the viscosity of this mush is low enough, i.e., where segregation processes have redistributed melts as discussed above, these along-axis portions of the lower crust may convect, transferring heat from the lower to the upper gabbroic crustal section and to the basaltic crust above. When the rising material reaches the top of the mush layer, the flow lines rotate to concentrate inside the high melt content, low effective viscosity region at and beneath the AML. Similarly, the flow lines in downwelling plumes rotate close to the base of the mush layer, and the flow concentrates inside the bottom-seated, decompacted, low viscosity horizon that

develops at and just above the transition between the crust and the upper mantle. This flow path describes the four limbs of the convective cell. We propose that the horizontal extension of this convective zone, defining a "corridor" embedded in the crustal low velocity zone of *Dunn et al.* [2000] is, at first-order, similar to the width of the AML and in the range 0.5–1 km. In three-dimensions, the convective magmatic cells can thus be seen as "wheel rims" filled with viscous material for which we infer a low effective viscosity, down to $10^{11}$ Pa.s because of the combined effects of high melt content and high strain rate. These wheels are several kilometers-deep and long, a few hundreds of meters to a kilometer-wide and centered right at the ridge axis. The inner cores of the wheels/cells are domains of lower crustal material with less melt, smaller strain-rate, and higher effective viscosity ($>10^{16}$ Pa.s) (Figure 1b). This circulation in the lower crust interacts thermally with the hydrothermal circulation in the brittle upper crust, with convective modes influencing each other in each layer. These modal/thermal interactions are described and studied numerically in the next sections.

## 3. Mathematical, Physical, and Numerical Models

### 3.1. Model Setup, Boundary and Initial Conditions, and Numerical Techniques

Our simplified model geometry (Figure 1b) is 18 km long and 6 km deep so that a complete vertical cross-section typical of fast-spreading ridges (Figure 1a) is represented, from the seafloor down to the Moho. The model temperature domain is (4–1250°C).

#### 3.1.1. Mass Transfer in the Hydrothermal Layer

The hydrothermal system is defined between 4°C and $T_{cut} = 800°C$ which is the temperature of the brittle-ductile transition for basaltic rocks [*Hirth et al.*, 1998]). Fluid flow obeys to Darcy's law. We use a single-phase flow formalism in which seawater flows in the single-phase area while only the "vapor-like" fluid moves along the convective path in the two-phase area ("brine-like" fluids are considered immobile). Mass conservation and fluid flow are given by

$$\nabla.(\rho_H V_H)=0 \tag{3}$$

$$V_H=-K_H/\mu_H(\nabla P+\rho_H g) \tag{4}$$

$V_H(U_H,W_H)$ is the fluid Darcy velocity vector in two-dimension, $K_H$ is the crust permeability, $\mu_H$ and $\rho_H$ are the hydrothermal fluid viscosity and density, respectively, $g$ is the gravity vector (coordinate z upwards), and P is pressure. We neglect in equation (3) the transient density variation term. We introduce the hydrothermal stream function $\Psi_H$ that satisfies

$$\rho_H U_H=\partial_z \Psi_H \tag{5}$$

$$\rho_H W_H=-\partial_x \Psi_H \tag{6}$$

Now, eliminating P taking the curl of equation (4), $\Psi_H$ verifies

$$R^{-1}\Delta\Psi_H=-(\partial_x R^{-1} \cdot \partial_x \Psi_H+\partial_z R^{-1} \cdot \partial_z \Psi_H)+\partial_x \rho_H \tag{7}$$

where R is the fluid hydraulic resistivity ($R = K_H\rho_H g/\mu_H$), $\partial_i$ represents the spatial derivative in direction i (Einstein notation), and $\Delta$ is the Laplacian operator. The hydraulic resistivity R is calculated using realistic, seawater-based, temperature and pressure-dependent fluid properties (viscosity, density, heat capacities) [e.g., *Fontaine and Wilcock*, 2007]. Equation (7) is made dimensionless and solved on a $256 \times 768$ numerical grid, following the numerical procedure described by *Douglas and Rachford* [1956] for parabolic equations. This stream function is set to zero on the $T_{cut} = 800°C$ interface, at the base of the hydrothermal layer [*Fontaine et al.*, 2011]. We define the numerical hydrothermal Rayleigh number $Ra_{H-num}$ which controls the vigor of convection in the hydrothermal layer as:

$$Ra_{H-num}=\Delta\rho_H g H K_H/\mu_{Hr}\kappa \tag{8}$$

where $\Delta\rho_H$ is the density contrast between hot and cold fluids, H is the thickness of the whole layer, $K_H$ is the permeability of the hydrothermal layer, and $\mu_{Hr}$ is the reference viscosity of hot hydrothermal fluids (see Table 1 for parameter values).

#### 3.1.2. Mass Transfer in the Magmatic Layer

Mass transfer in the magmatic layer is modeled between $T_{melt} = 1050°C$ and 1250°C. We consider a simplified flow formalism for the magmatic convection and use the Boussinesq approximation and a constant

viscosity fluid. These simplifications should however lead to a good first-order approximation of the channelized, "wheel rim" flow of our conceptual model as it is known from historical models of convective flows that even in the case of constant viscosity fluids, the flow tends to concentrate at the periphery of the convective cells [e.g., *McKenzie et al.*, 1974; *Parmentier et al.*, 1976; *Parmentier*, 1978]. The equations governing the convective flow in the magmatic layer are:

$$\nabla.(V_M)=0 \tag{9}$$

$$\Delta^2\Psi_M=-\rho_M g\alpha_M(\mu_M)^{-1}-\partial_x T \tag{10}$$

where $V_M(U_M, W_M)$ is the magmatic velocity vector in two dimension, $\Delta^2$ is the bi-Laplacian operator and $\psi_M$ is the magmatic stream function derived from Navier-stokes flow law and verifies

$$U_M=\partial_z\Psi_M \tag{11}$$

$$W_M=-\partial_x\Psi_M \tag{12}$$

Equation (10) is made dimensionless and solved on the $256 \times 768$ grid using the formalism published by *Conte and Dames* [1958] for biharmonic/elliptic equations. This stream function is also set to zero on $T_{melt} = 1050°C$. A similar approach is published and detailed in *Petitjean et al.* [2006]. We define the numerical magmatic Rayleigh number $Ra_{M-num}$ which control the vigor of convection in the model magmatic layer as:

$$Ra_{M-num}=\rho_M\Delta T_M\alpha_M gH^3/\mu_M\kappa \tag{13}$$

Note that the definition of $Ra_{M-num}$ in equation (13) differs from the one of $Ra_M$ in equation (1) as for the purpose of modeling the two-layers, hydrothermal-magmatic system, one has to consider the whole layer thickness H.

### 3.1.3. Heat Transfer in the Whole, Two-Layer Model

While flows follow specific and different laws in the hydrothermal and magmatic layers, heat transfer is controlled by a single advection-diffusion equation for the whole system

$$\partial_t T+\gamma V_{H,M}\bullet\nabla T=\kappa\Delta T \tag{14}$$

where $\partial_t$ is the time derivative, T is the temperature (fluid-rock thermal equilibrium is considered in the hydrothermal layer), and $\kappa$ is the crust effective diffusivity. $V_{H,M}$ is the fluid velocity vector in the hydrothermal or magmatic layer, i.e., $V_{H,M}= V_H$ when $T\in[2–800°C]$, $V_{H,M}=V_M$ when $T\in[1050–1250°C]$, and $V_{H,M}= 0$ when $T\in[800–1050°C]$. Accordingly, in between the two convective layers, there is a thermal, conductive (no flow) layer in which the temperature ranges between 800°C (i.e., $T_{cut}$) and 1050°C (i.e., $T_{melt}$). $\gamma = \gamma(T,P) = (\rho C_p)_{H \text{ or } M}/(\rho C_p)^*$, where "*" refers to the crust. $\gamma$ only influences fluid flow in the hydrothermal layer as $(\rho C_p)_H$ differs significantly from $(\rho C_p)^*$ at temperature $> 400°C$ [*Fontaine and Wilcock*, 2007], but equals 1 in the magmatic layer. We neglect the pressure-work term in equation (14). Equation (14) is solved using a finite-difference, fully implicit scheme derived by *Douglas and Rachford* [1956].

### 3.1.4. Boundary and Initial Conditions

We consider an open-top system in which the fluid (seawater) is free to enter or exit ($\partial_z T = 0$ or $T = 4°C$, when seawater flows out or in at the top of the model box, respectively). The base of the whole model domain set at 1250°C is free-slip ($\psi_M = \partial^2_z\psi_M = 0$). The top of the magmatic layer at $T = T_{melt} = 1050° C$ is no-slip ($\psi_M =\partial_z\psi_M = 0$). We impose $\psi_H = 0$ at the base of the hydrothermal layer where $T = T_{cut} =800°C$. Side boundaries assume periodic conditions. This ensures that the model magmatic and hydrothermal convective wavelengths are not forced by lateral/side boundary conditions. Simulations are initiated with a linear, conductive profile from 4°C to 800°C in the first upper 2 km of the modeling box and a constant temperature of 1250°C in the lower 4 km with a step increase in temperature from 800°C to 1250°C at a depth of 2 km. A small random thermal perturbation is applied to the total temperature field to trigger convective instabilities.

In each layer, the vigor of convection is controlled by their respective numerical Rayleigh number: $Ra_{H-num}$ and $Ra_{M-num}$. We also introduce the Nusselt number as the dimensionless temperature gradient at the base of the modeling box

$$Nu = \int\limits_{0}^{1} \left.\frac{\partial \theta}{\partial z'}\right|_{z'=0} \Delta x' \qquad (15)$$

where $\theta$ and $\Delta x'$ are the dimensionless temperature and grid size, respectively. When Nu = 1, the heat is transferred by pure conduction in the magmatic layer and when Nu > 1, then heat is also transferred by advection processes. We systematically vary $Ra_{H-num}$ and $Ra_{M-num}$ in order to test the effects of brittle crust permeability and lower crust viscosity, respectively. In particular, we quantify how these two parameters control the depth to the model AML roof and heat flux of vents, two characteristics that can be derived from seismic experiments and from seafloor observations at hydrothermal sites [see e.g., *Lowell et al.*, 2013 and references herein], respectively.

### 3.2. Modeling Results: Conduction-Dominated Upper Crust

In this section, we discuss models in which the upper porous crustal layer is conductive ($Ra_{H-num} = 0$). Although, this series of models is not realistic from the geologic point of view, it gives some insights into the primary characteristics of the convective magmatic system alone. In Figure 2 we show the results of an experiment in which only the magmatic layer convects with a Rayleigh number $Ra_{M-num} = 10^7$. The simulation reaches steady state with a Nusselt number that stabilizes around Nu = 1.7. The flow is composed of four convective cells (i.e., two upflow zones) in the magmatic layer. In the upper, conductive layer, the isotherms are deflected toward the top of the model box above magmatic upflows, while they deepen above magmatic downflows. The $T_{cut}$ interface at the base of the upper conductive layer is found at a depth of ~2830 and ~2180 m below the model top surface above magmatic downflows and upflows, respectively. Increasing the vigor of magmatic convection leads to shallower depths to the $T_{cut}$ interface and accordingly to a thinner upper conductive layer. For instance, when $Ra_{M-num} = 10^8$, the thickness of the conductive layer is ~1320 m and ~1640 m above magmatic upflow and downflow, respectively (Table 2).

We run simulations for the whole range of magmatic Rayleigh numbers discussed above, from the critical value of $Ra_{M-num} = 1300$ to the ~$10^8$ maximum value derived from our analysis of the lower crust effective viscosity $\mu_M$ (i.e., $10^{11}$–$10^{16}$ Pa.s). Most models reach steady state with Nu stabilizing at an asymptotic value, except solutions for $Ra_M = 10^8$, for which Nu has small fluctuations. We find that for values of $Ra_{M-num}$ lower than a critical value of $2 \times 10^6$, the Nusselt number never exceeds 1, indicating that heat transfer in the magmatic layer is purely diffusive. This is because convective instabilities do not have time to arise in the magmatic layer as it cools and thins from above by diffusion. We show in Figure 3 the temporal evolution of the "equivalent" numerical magmatic Rayleigh number, $Ra_{M-num/eq}$ ($Ra_{M-num/eq} = Ra_{M-num} \times (H-D_M)/H$, $D_M$: depth to the top of the magmatic layer in the models, see Table 2) which is $Ra_{M-num}$, corrected by the effective magmatic layer thickness at steady state, for three simulations at $Ra_{M-num} = 10^6$, $2 \times 10^6$ and $3 \times 10^6$. Interestingly, for a $Ra_{M-num}$ lower than $2 \times 10^6$, the equivalent Rayleigh decreases very quickly with time and stabilizes at an asymptotic value close to the critical Rayleigh number of 1300 for single layer convection with free-slip and no-slip bottom and top boundary conditions, respectively. We also test the effects of initial conditions on the arising of convective instabilities in the magmatic layer and initiate a $Ra_{M-num} = 10^6$ experiment with the stabilized, steady state final thermal convective field of a $Ra_{M-num} = 3 \times 10^6$ experiment. We find that this initial convective thermal field
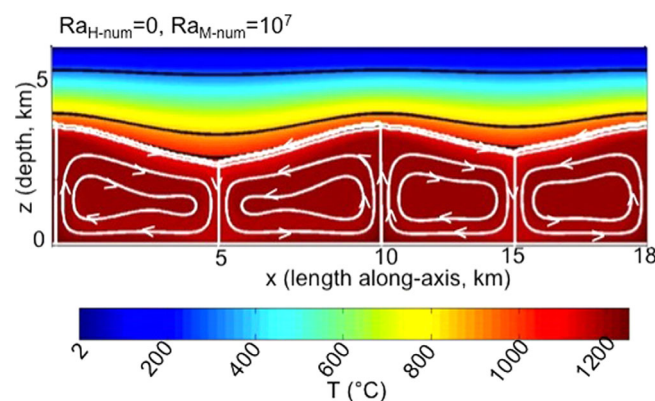


**Figure 2.** Steady state results for a numerical experiment with $Ra_{M-num} = 10^7$ and $Ra_{H-num} = 0$. The shading represents the vertical temperature field in the whole domain. Thick black lines represent the 300°C, $T_{cut} = 800$°C and $T_{melt} = 1050$°C isotherms (from the top to the bottom of the model box). White lines show selected flow lines (i.e., stream function isolines) and arrows indicate flow direction. As $Ra_{H-num} = 0$ here, fluid flow occurs only in the magmatic layer (white lines only in model domains where the temperature ≥ 1050°C).

**Table 2.** Summary of Numerical Simulations

| | $Ra_{M-num} = 5 \times 10^6$ | $Ra_{M-num} = 10^7$ | $Ra_{M-num} = 10^8$ |
|---|---|---|---|
| $Ra_{H-num} = 0$[a] | $D_M$[b] $= 3.23 - 4.43$<br>$D_H$[c] $= 2.63 - 3.18$<br>$\Delta H$[d] $= 0.6 - 1.24$<br>$Nu$[e] $= 1.39$<br>$Nu_{top}$[f] $= 1.4$<br>$Ra_{M-num/eq}$[g] $= [0.9 - 4.9] \times 10^5$<br>$Q_{max}$[h] $= 0.77$ W/m$^2$ | $D_M = 2.72 - 3.87$<br>$D_H = 2.21 - 2.86$<br>$\Delta H = 0.51 - 1.02$<br>$Nu = 1.67$<br>$Nu_{top} = 1.71$<br>$Ra_{M-num/eq} = [0.4 - 1.6] \times 10^6$<br>$Q_{max} = 0.92$ W/m$^2$<br>Figure 2 | $D_M = 1.66 - 2.1$<br>$D_H = 1.32 - 1.64$<br>$\Delta H = 0.34 - 0.47$<br>$Nu = 2.88$<br>$Nu_{top} = 2.88$<br>$Ra_{M-num/eq} = [2.7 - 3.8] \times 10^7$<br>$Q_{max} = 1.59$ W/m$^2$ |
| $Ra_{H-num} = 50$ | N/A | $D_M = 2.54 - 3.92$<br>$D_H = 1.98 - 2.9$<br>$\Delta H = 0.51 - 0.92$<br>$Nu = 1.71$<br>$Nu_{top} = 1.72$<br>$Q_{max} = 2.5$ W/m$^2$<br>$Ra_{H-num/eq} = 16.53 - 24.23$<br>$Ra_{M-num/eq} = [0.4 - 1.9] \times 10^6$<br>$K_{H/eq}$[i] $= 8.3 \times 10^{-17}$ m$^2$ | $D_M = 1.34 - 2.03$<br>$D_H = 1.02 - 1.57$<br>$\Delta H = 0.28 - 0.51$<br>$Nu = 2.64 - 3.46$<br>$Nu_{top} = 3.22$<br>$Q_{max} = 3.78$ W/m$^2$<br>$Ra_{H-num/eq} = 8.46 - 13.07$<br>$Ra_{M-num/eq} = [2.9 - 4.7] \times 10^7$<br>$K_{H/eq} = 8.3 \times 10^{-17}$ m$^2$ |
| $Ra_{H-num} = 100$ | N/A | $D_M = 2.58 - 4.15$<br>$D_H = 1.98 - 3.18$<br>$\Delta H = 0.51 - 0.87$<br>$Nu = 1.76$<br>$Nu_{top} = 1.8$<br>$Q_{max} = 2.88$ W/m$^2$<br>$Ra_{H-num/eq} = 33 - 53$<br>$Ra_{M-num/eq} = [0.3 - 1.84] \times 10^6$<br>$K_{H/eq} = 1.7 \times 10^{-16}$ m$^2$<br>Figure 4 | $D_M = 1.38 - 2.31$<br>$D_H = 1.06 - 1.85$<br>$\Delta H = 0.32 - 0.51$<br>$Nu = 2.73 - 3.65$<br>$Nu_{top} = 3.17$<br>$Q_{max} = 3.97$ W/m$^2$<br>$Ra_{H-num/eq} = 17.7 - 30.76$<br>$Ra_{M-num/eq} = [2.3 - 4.6] \times 10^7$<br>$K_{H/eq} = 1.7 \times 10^{-16}$ m$^2$<br>Figure 5a |
| $Ra_{H-num} = 200$ | N/A | No solution:<br>Hydrothermal system cools<br>entirely the magma layer | $D_M = 1.34 - 2.35$<br>$D_H = 0.97 - 1.85$<br>$\Delta H = 0.28 - 0.51$<br>$Nu = 2.4 - 3.7$ (3.12)<br>$Nu_{top} = 3.4$<br>$Q_{max} = 6.1$ W/m$^2$<br>$Ra_{H-num/eq} = 32.3 - 61.5$<br>$Ra_{M-num/eq} = [2.2 - 4.7] \times 10^7$<br>$K_{H/eq} = 3.3 \times 10^{-16}$ m$^2$<br>Figure 5b |
| $Ra_{H-num} = 500$[j] | N/A | No solution:<br>Hydrothermal system cools<br>entirely the magma layer | $D_M = 1.8 - 4.8$<br>$D_H = 1.3 - 4.3$<br>$\Delta H = 0.23 - 0.78$<br>$Nu = 4.24$<br>$Nu_{top} = 6.50$<br>$Q_{max} = 32.3$ W/m$^2$<br>$Ra_{H-num/eq} = 107.7 - 357.7$<br>$Ra_{M-num/eq} = [0.08 - 3.43] \times 10^7$<br>$K_{H/eq} = 8.3 \times 10^{-16}$ m$^2$<br>Figure 5c |

[a]$Ra_{H-num/eq}$: Range of equivalent hydrothermal Rayleigh number ($Ra_{H-num} \times D_H/H$).
[b]$D_M$(km): minimum and maximum depths to the top of the magmatic layer (1050°C isotherm) from the top of the model box.
[c]$D_H$(km): minimum and maximum depths to the base of the hydrothermal layer (800°C isotherm) from the top of the model box.
[d]$\Delta H$ (km): minimum and maximum thicknesses of the layer between the top/hydrothermal and bottom/magmatic layers in the 800–1050°C range.
[e]$Nu$: Nusselt number (dimensionless) at the bottom of the model box = mean dimensionless conductive heat flux along the model base. Equation (15).
[f]$Nu_{top}$: Nusselt number (dimensionless) at the top of the model box = mean dimensionless conductive heat flux + mean dimensionless advective heat flux along the model top.
[g]$Ra_{M-num/eq}$: Range of equivalent magmatic Rayleigh number ($Ra_{M-um} \times (H - D_M)/H$).
[h]$Q_{max}$: maximum heat flux density (W/m$^2$) along the top interface. When $Ra_{H-num} > 0$, $Q_{max}$ represents the maximum vent heat flux; when $Ra_{H-num} = 0$, it is the maximum conductive heat flux.
[i]$K_{H/eq}$: Equivalent hydrothermal system permeability (m$^2$).
[j]This model has not reach steady state and hydrothermal cooling is still active and thins the magmatic layer.

returns progressively to a diffusive one as the Nusselt number and $Ra_{M-num/eq}$ decrease and the magmatic layer thins. This shows that our results are independent of initial conditions, and that convective instabilities in the lower crust cannot be sustained at $Ra_{M-num}$ lower than $\sim 2 \times 10^6$.
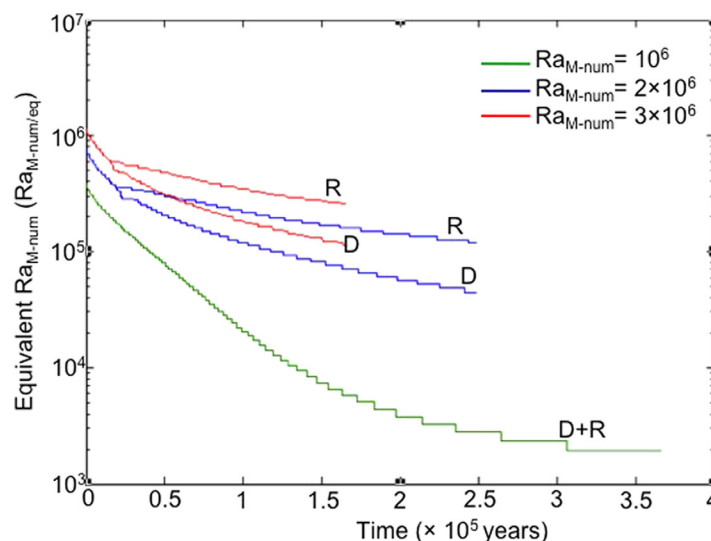
**Figure 3.** Temporal evolution of the equivalent Rayleigh numbers in magmatic recharge/downflow (R) and discharge/upflow (D) zones for three numerical experiments with $Ra_{H-num} = 0$. Only When $Ra_{M-num}$ is $> 2 \times 10^6$, can convection modes arise in the lower magmatic layer.

### 3.3. Modeling Results: Convection-Dominated Upper Crust

In this section, we present simulations obtained for the range of $Ra_{M-num}$ discussed above but for an upper layer that is also convecting with $Ra_{H-num}$ in the range [50–500]. For a given $Ra_{M-num}$, all simulation runs are initiated with the thermal field obtained from simulations with the same $Ra_{M-num}$ but with $Ra_{H-num} = 0$ (i.e., the final thermal field obtained in the "conduction-dominated" upper crust experiments discussed in the previous section). In Figure 4 we show the results of a simulation in which $Ra_{M-num} = 10^7$ and $Ra_{H-num} = 100$. The flow is still composed of four magmatic cells in the lower crust producing two magmatic upflows, and the combination of higher hydrothermal heat flux and shallower hydrothermal layer above magmatic upflows has led to the formation of four large, 4 to 5 km-long hydrothermal cells producing two upflows in the upper hydrothermal layer. Interestingly, the centers of the hydrothermal and magmatic upflows are offset by $\sim$ 1300 m. This is because the base of the hydrothermal layer (i.e., the $T_{cut}$ isotherm) has a slope as a result of the magmatic-hydrothermal couplings: hydrothermal upflows tend to arise upslope next to zones where the $T_{cut}$ isotherm shoals and flattens.

Increasing $Ra_{M-num}$ (e.g., Figure 5a, $Ra_{H-num} = 100$ but $Ra_{M-num} = 10^8$) leads to a shallower and smoother $T_{cut}$ interface (Table 2), but the hydrothermal and magmatic layers are still strongly coupled and the hydrothermal cells produced are still 4 to 5 km-long. When increasing $Ra_{H-num}$ (e.g., when $Ra_{H-num} = 200$ and $Ra_{M-num} = 10^8$, figure 5b), other hydrothermal upflow zones form transiently. The appearance of this transient behavior in the hydrothermal layer marks a transition from a magmatically dominated coupled system to a hydrothermally dominated one when $Ra_{H-num} = \sim 200$. When $Ra_{H-num} < \sim 200$, the wavelength of hydrothermal cells is controlled by the wavelength of the magmatic cells and hydrothermal upflows arise near the center of the magmatic upflows. When $Ra_{H-num} > \sim 200$ (e.g., Figure 5c), hydrothermal cooling produces perturbations with shorter wavelengths on the $T_{cut}$ interface and smaller hydrothermal cells tend to arise. This leads to the production of hydrothermal upflow zones away from magmatic upflow zones, and the modal couplings between the hydrothermal and magmatic layer is therefore weaker. In this regime, hydrothermal circulation is also able to influence the convective wavelength in the magmatic layer: the magmatic cells become shorter along-axis as the magmatic layer is thermally eroded by hydrothermal cooling from above (Figure 5c).
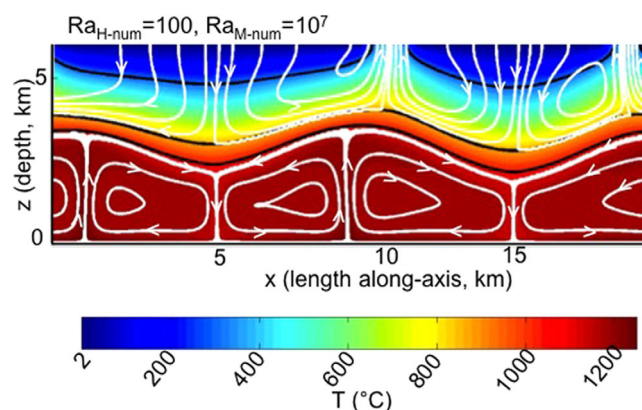


**Figure 4.** Same as Figure 2 but with $Ra_{M-num} = 10^7$ and $Ra_{H-num} = 100$. Hydrothermal and magmatic flows occur in model domains where $T < 800°C$, and $T \geq 1050°C$, respectively.

Because of hydrothermal cooling, the depth to the base of the hydrothermal layer ($T_{cut}$) increases below hydrothermal recharge and reaches $\sim 3180$ m
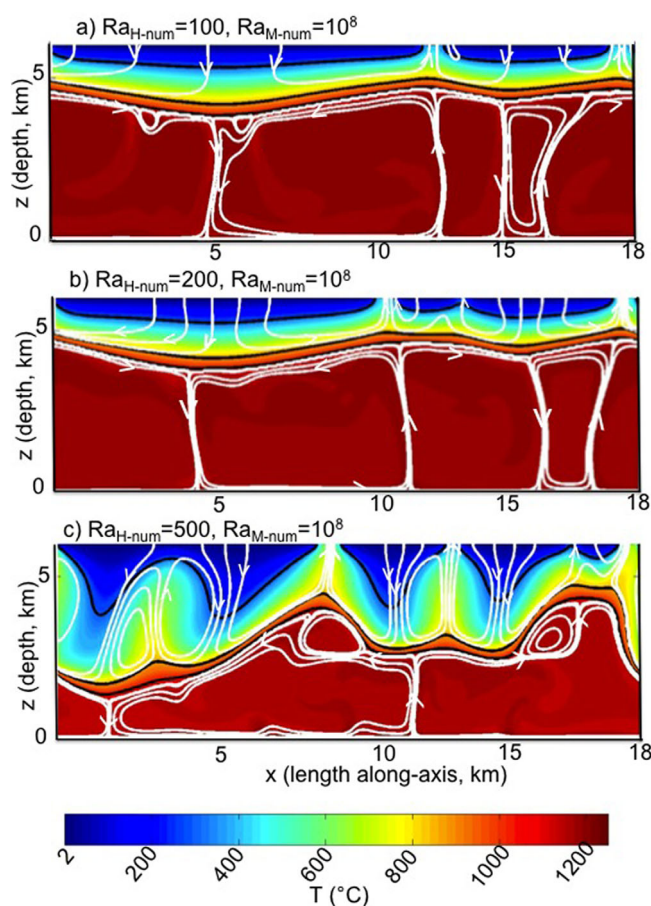
**Figure 5.** 2-D temperature distribution in the whole modeling domain for various $Ra_{M-num}$-$Ra_{H-num}$ couples. (a) $Ra_{M-num} = 10^8$, $Ra_{H-num} = 100$. (b) $Ra_{M-num} = 10^8$, $Ra_{H-num} = 200$. (c) $Ra_{M-num} = 10^8$, $Ra_{H-num} = 500$. When $Ra_{H-num} \geq 200$, the two layers are weakly coupled.

when $Ra_{M-num} = 10^7$ and $Ra_{H-num} = 100$ (Figure 4) compared to $\sim$2860 m when $Ra_{H-num} = 0$ (Figure 2). However, below the hydrothermal discharge the hydrothermal layer is $\sim$250 m shallower in Figure 4 when $Ra_{H-num} = 100$ than in Figure 2 when $Ra_{H-num} = 0$ (Table 2). This is because hydrothermal convection advects isotherms upward in upflow zones. As said above, for a given $Ra_{M-num}$, all simulations run with $Ra_{H-num} \neq 0$ are initiated with the final "converged" thermal field of a simulation with the same $Ra_{M-num}$ but with $Ra_{H-num} = 0$. For any $Ra_{M-num}$ considered, and for $Ra_{H-num}$ lower than the critical $Ra_{H-num}$ of $\sim$200, the magmatic/hydrothermal dynamical couplings adjust the steady state position of the $T_{cut}$ interface at a shallower depth below discharge compared to the depth induced by the initial condition. When $Ra_{H-num} > 200$, hydrothermal convection is vigorous enough to cool the lower magmatic layer below hydrothermal discharge and for a fixed $Ra_{M-num}$ the $T_{cut}$ interface settles deeper and deeper when increasing $Ra_{H-num}$.

All simulations with $Ra_{H-num} \leq 200$ (strongly coupled hydrothermal and magmatic layers), reach (quasi-) thermal equilibrium, i.e., the mean heat Nu entering at the base of the system is extracted at the top ($Nu_{top}$, Table 2). In these models the maximum venting temperatures during the simulation is $\leq$420°C. This maximum temperature is in agreement with thermodynamical considerations stating that venting temperatures cannot exceed the value at which the fluxibility of the circulating fluids is maximum [e.g., *Jupp and Schultz*, 2000; *Geiger et al.*, 2005; *Coumou et al.*, 2008]. This temperature depends on the salinity of the fluids and on the pressure at the base of the system. In our models, we use seawater-like (3.2 wt.% NaCl) fluid properties, and the maximum pressure reached by the fluids ranges between 300 and 500 bars. In *Geiger et al.* [2005] it is shown that for such salinity and pressure range, the fluxibility is maximum at a temperature of 430–440°C. A better description of the model venting temperatures, more consistent with data collected along fast-spreading ridges (<380°C at EPR-9°50′N) [e.g., *VonDamm et al.*, 2004] would require the development of two-phase, NaCl-H2O flow. Simulations with $Ra_{H-num} = 500$ do not reach thermal equilibrium and the hydrothermal and magmatic layers are decoupled (Figure 5c). In these simulations, maximum venting temperatures are >500°C. This could result from the simplified flow formalism that we use in the hydrothermal layer. Neglecting transient density variations in the mass conservation equation (equation (3)) and pressure work (an additional term accounting for transient pressure variations in the temperature equation), likely results in "overshooting" issues and unrealistically high flow temperatures when the hydrothermal circulation is too vigorous in the hydrothermal layer. According to the fluxibility argument, these additional terms would tend to limit the buoyancy of hot fluids (500–800°C) at the base of the system, keeping them in the bottom boundary layer [*Jupp and Schultz*, 2000; *Geiger et al.*, 2005; *Coumou et al.*, 2008]. These "overshooting" issues do not seem to influence flow dynamics and geometry of our strongly coupled models ($Ra_{H-num} < 200$) as model venting temperatures are thermodynamically consistent. This is probably due to the fact that in these models the friction

forces win over the buoyancy forces at the bottom of the box because of the low $Ra_{H-num}$ and associated permeability.

Table 2 summarizes the model depth to the base of the hydrothermal layer for all simulations. It also summarizes the thicknesses $\Delta H$ of the conductive zone between the top of the magmatic domain at 1050°C and the bottom of the hydrothermal domain at 800°C. For the range of $Ra_{H-num}$ and $Ra_{M-num}$ considered in this section, $\Delta H$ minimum thicknesses below model vent fields range between ∼270m when $Ra_{M-num} = 10^8$ and $Ra_{H-num} = 200$, and ∼400 m when $Ra_{M-num} = 10^8$ and $Ra_{H-num} = 0$ (i.e., conduction-dominated upper crust). This corresponds to a mean heat flux at the base of the hydrothermal layer of 0.5–1 W/m$^2$ (Nu*$\Delta$T/H ∼3*1246/6000, see Table 2). Considering our 18 km-long model box, and a heat uptake area limited to the across-axis width of the AML (500–1000 m), the hydrothermal circulation modeled here therefore transports 10–20 MW. This heat is partitioned between 2 and 3 vent fields, so that their maximum heat flux is only about 10 MW each.

## 4. Discussion

### 4.1. Strong Versus Weak Magmatic-Hydrothermal Coupling

In the coupled convective fluid-porous system, we envision for fast-spreading axes, the axial thermal regime, and crustal temperature distribution are controlled by the balance between hydrothermal cooling and mush convection, i.e., by the effective mush viscosity and by the permeability of the upper crustal layer, $\mu_M$ and $K_H$, respectively. The possible range of $\mu_M$ is constrained by our discussion of lower crust melt distribution and its redistribution by melt segregation processes (section 2). In the upper crust, the model permeability is linearly linked to the hydrothermal Rayleigh number $Ra_{H-num}$. In our models, to obtain thicknesses of the hydrothermal and magmatic layers that are typical of fast ridges, i.e., 1–2 km and 4–5 km, respectively, the Rayleigh number of the top hydrothermal layer $Ra_{H-num}$ cannot exceed a value ∼200.

The depth to the AML, as determined by seismic experiments, constrains the depth to the top of the magmatic layer ($T_{melt} = 1050$°C isotherm in our experiments). Our models predict that the along-axis position of this isotherm is not constant, being deeper at hydrothermal recharge zones than at discharge ones. This along-axis depth variation ranges from 440 m and up to 1 km over 8–10 km along-axis when $Ra_{M-num} = 10^8$. Values of a very few hundreds of meters at the lower end of our model range are more realistic for fast-spreading ridges [e.g., *Carbotte et al.*, 2013]. However, in our models, for a given $Ra_{H-num}$ this along-axis depth variation is decreasing when increasing $Ra_{M-num}$ (Table 2). We calculate with equation (1) that the maximum Rayleigh number of the actual axial magma chamber ($Ra_M$) should be about $10^8$, but we run simulations with maximum equivalent numerical magmatic Rayleigh ($Ra_{M-num/eq}$) about one order of magnitude lower because of the effect of having the magmatic system convecting only in the lower part of the system (Table 2). Following the trend found in our models that shows that one order of magnitude in $Ra_{M-num}$ between $10^7$ and $10^8$ results in a reduction by a factor >2 of the predicted AML depth difference (Table 2), raising $Ra_{M-num/eq}$ by an order of magnitude to reach the value of $10^8$, would lead to values of a few hundreds of meters, more in agreement with observations of along-axis AML depth variations at fast-spreading ridges [e.g., *Carbotte et al.*, 2013].

As we have defined an equivalent numerical magmatic Rayleigh ($Ra_{M-num/eq}$), it is also customary and more meaningful to consider an equivalent hydrothermal Rayleigh number $Ra_{H-num/eq}$, which is $Ra_{H-num}$ corrected by the actual thickness of the hydrothermal layer obtained in the models ($Ra_{H-num/eq} = Ra_{H-num} \times D_H/H$; $D_H$: depth to the base of the hydrothermal layer, see Table2). In our simulations with $Ra_{H-num} < \sim200$, $Ra_{H-num/eq}$ ranges between 8 and 32 and 13 and 61, in discharge and recharge zones, respectively. These values are lower or just a few times higher than the critical Rayleigh number of 26 for convection to arise in an open-top porous layer with a constant temperature bottom boundary [*Cherkaoui and Wilcock*, 1999]. Moreover, in our definition of $Ra_{H-num}$ (equation (8)) we use the viscosity of "hot" hydrothermal fluids (>300°C), which means that our range of $Ra_{H-num/eq}$ correctly characterizes hydrothermal upflow zones, but is overestimated in cold downflow zones. For example in our experiment with $Ra_{H-num} = 200$ ($Ra_{H-num/eq} = 32.3–61.5$, Table 2) and $Ra_{M-num} = 10^8$ (Figure 5b), the mean seawater viscosity in the downflow zone at x = 5000 m is about $1.8 \times 10^{-4}$ Pa.s, i.e., about three times greater than the reference viscosity of $5.1 \times 10^{-5}$ Pa.s used in $Ra_{H-num}$. Accordingly, the effective $Ra_{H-num/eq}$ in this downflow zone should be lower than the mean value of 61.5 listed for this experiment in Table 2 and would thus be close to, and even a little lower than the

critical Rayleigh for open-top systems. Inverting for k in equation (8) with the model range of $Ra_{H-num/eq}$ (see Table 2) the coupling between the magmatic and hydrothermal layers is strong, provided that the effective permeability of the hydrothermal layer is not exceeding $\sim 10^{-16}$ m$^2$.

The arising of hydrothermal convection in a layer with a Rayleigh number lower than critical could seem counterintuitive but *Wood and Hewett* [1982] have shown that it is possible when this layer is tilted. They describe a "weak" convective regime with a flow pattern composed of a steady unicellular motion in which the fluid moves upslope along the heated bottom boundary. When the Rayleigh number of the layer exceeds the critical value times the cosinus of the tilt, multicellular convection can arise. This is a situation very similar to the hydrothermal flow pattern obtained in our simulations. At $Ra_{H-num} < 200$ the effective Rayleigh of the hydrothermal layer is lower than critical. However, because of magmatic convection in the lower crust, the thickness of the hydrothermal layer defined by the depth to the $T_{cut}$ interface is not constant along-axis: it is thicker above magmatic downflows and thinner above upflows. Because of this bottom topography and of the associated lateral temperature gradients, a steady, unicellular, "background" convective flow pattern forms in the hydrothermal layer at the same scale of the magmatic cells underneath. When $Ra_{H-num} > 200$, the equivalent Rayleigh number in the hydrothermal layer is greater than critical and a multicellular, unsteady flow pattern arises as a result of local thermal instabilities in the bottom boundary.

A permeability of $\sim 10^{-16}$ m$^2$ as derived from our models, is about an order of magnitude lower than the value required to match AML depths in 2-D accretion models incorporating realistic hydrothermal flow [e.g., *Theissen-Krah et al.*, 2011, 2016]. One possible reason for this discrepancy between thermal models is the low Nusselt numbers (i.e., Nu $\cong$ 2-3) characteristics of our convective couplings. Our models describe the couplings between two superimposed convective systems "simply" heated from below for a range of permeability and viscosity. They do not incorporate additional heat sources like the latent heat of crystallization in the axial melt lens that increases the total heat available at the ridge axis. Models of cross-axis crustal accretion intrinsically incorporate some latent heat release at the top of the magmatic layer. Accordingly, more heat is available for hydrothermal circulation. In the initial cross-axis accretion models [e.g., *Morgan and Chen*, 1993], latent heat of crystallization is included and a higher Nu than in our simulations (i.e., Nu >8) is thus required to extract this heat and maintain the AMLs at realistic depths. For the same reasons, in the more sophisticated models incorporating cellular hydrothermal convection [*Theissen-Krah et al.*, 2011, 2016], a mean permeability of $\sim 10^{-15}$ m$^2$ is required.

### 4.2. Considerations on Melt Fluxes

Our models have implications for the possible geometry of melt delivery to the AML. Seismic studies indicate that the AML melt content is heterogeneous along-axis. At the EPR between 9°30′N and 10°N, *Xu et al.* [2014] show the presence of four, 2–4 km-long, melt-rich (melt content >70%) sections of the AML separated by ∼10kms-long, melt-poor (melt content <40%) sections. Along the Southern East Pacific Rise (SEPR) between 14°10′S and 14°30′S, *Singh et al.* [1998] found three, 2–4 km-long, regions of pure melt separated by about 15 km. In our models, the lower crustal crystal mush layer is ∼4 km-thick and ∼4 × 4 km-wide convective cells tend to form (e.g., Figures 5a and 5b). Accordingly, magmatic upwellings form every ∼ 8–9 kms. At the EPR, the observed separation length between zones of high melt content in the AML is thus commensurate with the 8–9 km spacing between our model magmatic upwellings. We therefore propose that the EPR AML could receive melt from the lower crust with a spatial periodicity controlled by the along-axis convective modes and distribution of magmatic upwellings in the gabbroic magma chamber (Figure 6). At the SEPR, the separation length between regions of pure melt in the AML (∼15 km) [*Singh et al.*, 1998] is significantly larger. Our model setup for the magmatic domain is however very simple (i.e., constant viscosity, Boussinesq fluid), favoring the formation of convective cells with aspect ratio ∼1. The AML is shallower along the SEPR (∼1 km below sea floor) [*Singh et al.*, 1998] than along the EPR-9°N (>1.5 km below sea floor) *Detrick et al.*, 1987], implying a thicker lower crust, and one may thus expect larger separation lengths between magmatic upflows. Variations in viscosity due to the presence of melt-rich, low-viscosity layers at the top and bottom of the gabbroic domain could also impact the length of the convective cells [*Richter and Daly*, 1978].

The mechanisms of melt transport/segregation from the gabbroic lower crust to the AML in our model are not well constrained but stresses due to magmatic convection could play a role. It has
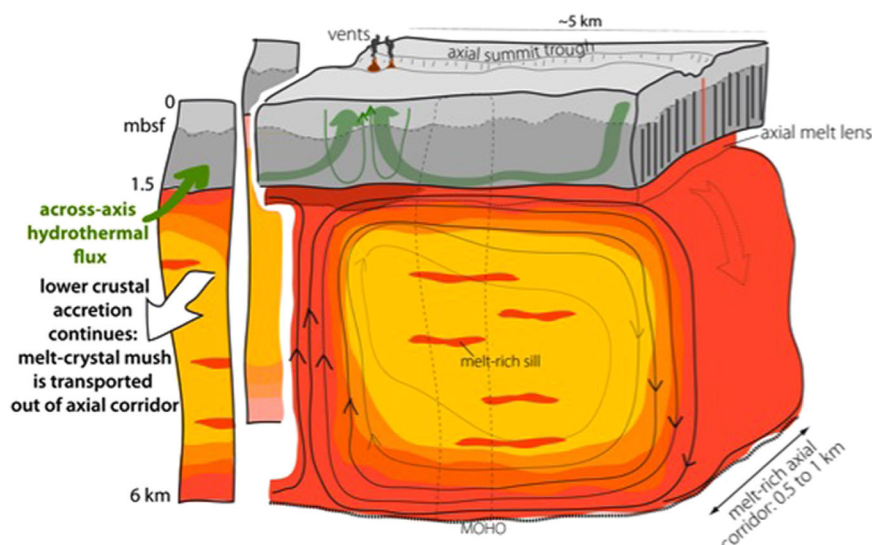
**Figure 6.** Sketch summarizing our conceptual model of magmatic and hydrothermal convective couplings at fast-spreading ridges. The lower crust (in yellow to red tones with grading from yellow to red indicating increasing melt content) convects along-axis as a viscous fluid in a narrow axial domain—or "corridor"—limited to the cross-axis AML extension. Lower crustal accretion continues as the crystal-melt mush formed in this corridor is transported and further cooled into each diverging plates. Magmatic convection cells in the corridor are 4–5km long and form "wheel rims" surrounding less melt-rich domains. Melt delivery to the AML is thus focused every 8–10 kms at the top of magmatic upflows (dark red area). Hydrothermal cells (in green) are strongly coupled to magmatic ones, and hydrothermal upflows located above magmatic upflows transport the latent heat due to melt crystallization in the AML. Additional heat can come from the cooling of the dyke and pillow sections above the AML and/or from the cooling of the whole gabbro section across-axis.

been shown that a primary control on melt trajectories is the direction of the most compressive principal stresses $\sigma 1$ [*Ceuleneer and Rabinowicz*, 1993; *Menand et al.*, 2010]. At the top of a viscous, two-phase, mushy upflow zone in a convective cell, $\sigma 1$ is vertical and horizontal tensile stresses develop as the flow rotates to concentrate in the top boundary layer [e.g., *Rabinowicz et al.*, 1987]. Although this process of melt migration from the magmatic plume toward the AML would require a more quantitative description of the thermomechanical couplings between melt segregation and magmatic convection, we argue that melts carried by the convective flow in the mushy gabbroic lower crust can segregate from the solid matrix to pool above the top of the upflow zone leading to "patches" of local melt enrichment.

In three-dimension, our model magmatic upflow zone is a pipe with a diameter of ∼1 km. The mean mass flux of magma through a horizontal section of this pipe equals: $\pi \times$(pipe radius)$^2 \times$ (mean melt concentration in the mush) $\times$ (mush vertical velocity, $W_M$) $= \pi \times (500)^2 \times (0.15) \times W_M = 1.2 \times 10^5 \times W_M$ m$^3$/s. In our model with Ra$_{M-num}$ $= 10^8$ (Figures 5), the mean upwelling velocity is about $10^{-6}$ m/s. Using this value as a first-order approximation of melt velocity, the mean, net magma flux through a pipe section is thus about $1.2 \times 10^{-1}$ m$^3$/s. This is very similar to the value of $1.6 \times 10^{-1}$ m$^3$/s estimated by *Lowell et al.* [2013] for AML replenishment rates at EPR 9°50′N.

### 4.3. Considerations on Vent Heat Fluxes

In our models, we do not take into account the latent heat release due to the crystallization of the lower crust as it is accreted. The models thus predict maximum vent heat fluxes of ∼10 MW corresponding to the modeled thickness of the boundary layer between the hydrothermal and magmatic convective systems (Table 2). This is about two orders of magnitude lower than estimates of heat fluxes at high-temperature mid-ocean ridge vent fields (e.g., EPR 9°50′N, Main Field Endeavour; see *Lowell et al.* [2013] and references herein for a compilation of known field heat fluxes).

Estimates of the steady state heat flux supplied to axial hydrothermal circulation by crustal accretion at fast-spreading ridges [*Mottl*, 2003; *Cannat et al.*, 2004] indicate that it ranges between 44 MW and 71 MW per km of ridge for a spreading rate of 10 cm/yr. This range depends on whether the axial hydrothermal circulation is restricted to the top of the upper axial magmatic lens (heat from dykes + melt specific heat + latent heat from gabbro crystallization) or affects the whole gabbro section. Our numerical simulations concern

the very near-axis "melt-rich corridor" below the AST (Figure 1) and are therefore explicitly set in the former case. Furthermore, we do not have access to the full heat of lower crust crystallization. Geological observations at the EPR indicate that most eruptions originate at or very near the Axial Summit Trough [*Fornari et al.*, 1998]. The production of MORB typical of the EPR (MgO ca. 7.3%) [*Rubin and Sinton*, 2007] requires ∼50% crystallization of a commonly proposed parent melt (KG1) [*Korenaga and Kelemen*, 1997] between 1256°C and 1146°C (calculation performed with the Petrolog software) [*Danyushevsky and Plechov*, 2011]. Assuming steady state accretion of a 6 km-thick magmatic crust, and a spreading rate of 10 cm/yr, we calculate that this releases ∼19 MW per km of ridge (heat from cooling between 1256° and 1146°C + latent heat for 50% crystallization). The lower crust magmatic convection cells, gathering heat on distance >4–5 km in the low-viscosity lower crust axial corridor can therefore deliver about 190 MW at the top of the km-wide magmatic upflows (1 upflow = 2 cells in 2-D). In addition, melt is injected as dykes into the upper crust, where it crystallizes fully and cools down to hydrothermal temperatures. For a 10 cm/yr spreading rate and a dyke layer thickness of 1.2 km, this should release an additional 14 MW per km of ridge into the hydrothermal domain. Our model hydrothermal cells are 4–5 km-long when the coupling between the hydrothermal and magmatic layers is strong (Figures 4, 5a, and 5b). Because the hydrothermal upflows are then near the underlying magmatic upflow zones, these cells can transport up to 330 MW to the vent sites, a value that is in the range of heat fluxes estimated at high-temperature EPR and Juan de Fuca vent fields [e.g., *Lowell et al.*, 2013 and references herein]. In addition, if across-axis hydrothermal cells also develop in the near-axis region, cooling the whole gabbro section to hydrothermal temperatures and merging into the along-axis hydrothermal cells modeled here [e.g., *Hasenclever et al.*, 2014], an additional heat flux of 38 MW per km of ridge (bringing the total heat flux to the 71 MW maximum estimate of *Mottl* [2003] and *Cannat et al.* [2004]) becomes available.

The gathering of such an amount of heat requires a local enhancement of the crustal permeability compared to our mean value of ∼$10^{-16}$ m$^2$ so that hydrothermal circulation/cooling can maintain the AML at realistic depths. In the model of *Lowell et al.* [2013], the formation of high-heat (i.e., ∝100 MW) fields at fast-spreading ridges requires that the crust has a permeability in the range $10^{-14}$–$10^{-12}$ m$^2$. This crustal permeability enhancement could result from local overpressures induced by active AML replenishment as proposed by *Wilcock et al.* [2009]. In our conceptual model, the AML receives melt from kilometer-wide magmatic upflows. Accordingly, the permeability enhancement required to evacuate magmatic heat concerns the hydrothermal domain overlying these upflows, and the ∼$10^{-16}$ m$^2$ permeability level can be inferred to prevail in the rest of the axial domain. In this configuration, local, subkilometer-sized hydrothermal cells restricted to the high-permeability areas, and regional, 5 to 10 km-long cells due to the larger-scale magmatic-hydrothermal couplings could merge to contribute to the production of high-heat vent fields (Figure 6).

### 4.4. Considerations on the Crystallization and Accretion of the Lower Crust

Two end-member models are usually invoked to explain the accretion/formation/crystallization of the lower crust: the "gabbro-glacier" (e.g., see the original models of *Morgan and Chen* [1993]) and the "sheeted-sills" [e.g., *Kelemen et al.*, 1997] models. In the "gabbro-glacier" model, primitive melts are delivered to the AML directly from the mantle. Most crystal nucleation and growth occurs within the AML and then a crystal mush subsides into the low-velocity zone to solidify even more and produce the lower crust. In the "sheeted-sills" model, primary mantle melts are trapped in multiple sills throughout the lower crust and crystallize in situ, in these sills, forming layered cumulates as observed in the Oman ophiolites [e.g., *Kelemen et al.*, 1997], while fractionated melts move upwards and pond at shallower levels. To reconcile the gabbro-glacier model with the occurrence of layered cumulates in the lower crust, *Buck* [2000] proposed that layered cumulates could also be made of crystals formed in the AML that would periodically sink down as slurries to settle as thin layers in deeper mushy domains. This "cumulate-descent" model requires an upper gabbro layer with a viscosity <$10^{10}$ Pa.s in the lower crust immediately below the AML, in a very near-axis domain that is equivalent to our "melt-rich corridor." "Hybrid" models in which the lower crust crystallizes partly in-situ and partly at AML level have also been proposed based on both petrological observations and thermal modeling [*Boudier et al.*, 1996; *Coogan et al.*, 2002; *MacLennan et al.*, 2004]. As summarized by *Perk et al.* [2007]: "...the basic physics of both models require some proportion of each process. In the gabbro glacier model, melt lubricates the subsiding crystal mush allowing it to flow; this melt is likely to crystallize in the deeper part of the crust. In the sheeted sill model the steeper thermal gradients, and thus more rapid

cooling, at shallow than deep levels in the crust requires some crystal subsidence to prevent the AMC from solidifying."

Our conceptual model (Figure 6) complements this hybrid model of accretion, in the sense that we propose that lower crustal accretion could occur in two stages, one, which we consider in the models, dominated by along-axis convection of melt-rich mushes in a narrow (0.5–1 km) corridor, and the other occurring outside this corridor, yet still within the 4–6 km-wide mush zone of *Dunn et al.* [2000]. In our models of the along-axis stage, melt is transported adiabatically from moho level by localized upflowing convective currents and delivered to portions of the AML where rapid partial crystallization occurs, producing residual melts with the composition of erupted MORB. The resulting cumulate may then sink down as proposed in the "cumulate-descent" model of *Buck* [2000], flow along-axis and down toward less dynamic regions away from the convecting "wheel rims," or be accreted in situ to the diverging plates. The effective viscosity of our convective wheel is commensurate with the viscosity of $\sim10^{10}$ Pa.s required in the cumulate-descent model [*Buck*, 2000]. As they sink down, the cumulates + melt slurries would interact thermally, mechanically, and chemically with the convective flow at the top of the magmatic layer and through the top thermal boundary layer where the flow is horizontal. Our models thus predict substantial along-axis variability of petrogenetic processes, with complex layering and strong magmatic foliations being more likely to be frozen into the diverging plates next to the wheel rims than in the less melt-rich regions inside the wheel rims. Such features have not been described in the gabbroic section of the Oman Ophiolite, which is commonly used as a fast-spreading-ridge analogue [e.g., *Boudier et al.*, 1996]. However, while direct sampling of fast spread EPR lower crust is very scarce, the EPR gabbros recently drilled at the Hess Deep trough show heterogeneity of lithologies, composition, type of layering, and deformation to a degree that is not found in the Oman Ophiolite gabbros [*Gillis et al.*, 2014]. These findings are not a validation of our convective lower crust hypothesis, yet they are not inconsistent with it, and do support the existence of complex and variable melt differentiation and crustal accretion processes in the lower crust at fast-spreading ridges [*Gillis et al.*, 2014].

Our model does not rule out the formation of melt-filled sills at the base [e.g., *Singh et al.*, 2006] and top (e.g., the "secondary AMLs" complex described by *Marjanović et al.* [2014]) of the axial lower crust as evidenced by seismic studies. Permeability barriers can indeed force melts to pond (see for example the 2-D numerical experiments by *Rabinowicz et al.* [2001]). Such permeability barriers could form in the axial lower crust of fast-spreading ridges due to the stress field induced by the mush convective motion: sills will preferentially form in regions where the most compressive principal stress is not vertical. More sophisticated models coupling melt segregation and convection with constraints from detailed analysis of the lower crust seismic structure would be required to understand these processes.

## 4.5. The Cases of Intermediate and Slow-Spreading Ridges

In this study we choose to focus on fast-spreading ridges because widespread seismic evidence and seafloor observations there indicate that the AML is a systematic and therefore presumably permanent feature. Our models definitely do not apply to the opposite case of slow-spreading ridges, where AML detections are both very rare and confined along-axis to 10 to 20 km-long volcanically robust ridge portions [e.g., *Singh et al.* 2006]. This seismic evidence concurs with findings from petrological studies [see *Coogan*, 2014], to indicate that melt bodies in slow-spread crust form transient intrusions [e.g. *Sinton and Detrick*, 1992]. AML detections are by contrast widespread along some intermediate spreading ridges, and our models may therefore be applicable there. The Endeavour segment of the Juan de Fuca Ridge is where the most robust constraints on hydrothermal and magmatic processes are available for an intermediate spreading ridge. The segment hosts five major high-temperature vent fields separated from each other by 2–3 kms. From south to north, the estimated heat fluxes of each individual fields are 114 MW, 297 MW, 368 MW, 64 MW, and 1MW [*Kellog*, 2011]. The intermediate spreading rate implies a more tectonically controlled and therefore higher overall crustal permeability than at the EPR because of faulting within the axial valley [e.g., *Johnson et al.*, 2010]. As a result, it may well be that at Endeavour, the Rayleigh number in the hydrothermal layer is above critical. If this is the case, and if the hydrothermal layer is coupled to a convective magmatic layer, our models predict that the wavelength of the convective cells in the hydrothermal layer would be shorter and no longer be controlled by the size of the magmatic cells, but by the permeability field. Moreover, this multicellular hydrothermal regime could influence and control the characteristics of the magmatic

cells (see discussion for Figure 5c in section 3). In the absence of robust constraints on melt distribution in the AML below the Endeavour hydrothermal fields, it is however difficult to test this hypothesis.

## 5. Conclusions

We study the possibility that the magmatic lower crust in the axial domain of fast-spreading ridges is unstable with regards to thermal convection. Weak, near-critical thermal convection requires mush viscosities of $\sim 10^{16}$ Pa.s to arise, consistent with the viscosity of a gabbro mush with a uniform melt content of 10%. We infer that more vigorous convective heat transfer is possible when further couplings between (i) on-going deformation induced by convective flow and (ii) melt segregation, lead to melt accumulation and viscosity reduction in the most sheared zones of the convection cells. These zones being the border of the upflow, downflow, top, and bottom horizontal conduits, the resulting convective flow can be seen as a "wheel-rim" filled with a low-viscosity ($10^{11}$–$10^{13}$ Pa.s) gabbro mush, transferring heat from moho level to the top of the gabbro pile. We propose that this thermal convection is confined within a narrow melt-rich "corridor," 0.5 to 1 km-wide across-axis, running along-axis below the axial melt lens and embedded within the low-velocity zone imaged by seismic tomography. We primarily focus on the impacts of this "magmatic" convection on hydrothermal convection in the upper fractured crust describing how magmatic and hydrothermal modes interact with each other. We develop a fully original and challenging 2-D numerical model coupling a "fluid-like" lower layer in which mass transfers are controlled by a Navier-Stoke flow equation, to a porous/permeable upper layer where mass transfers are controlled by a Darcy flow equation. We show that the two convective layers are strongly coupled (i.e., hydrothermal upflows arise above magmatic upflows) provided that the permeability of the top layer is not exceeding $\sim 10^{-16}$ m$^2$. In this case, magmatic and hydrothermal convection cells are 4 to 5 km-wide, so that vent fields are spaced by 8–10 km. We propose that this coupling could explain the distribution of high-temperature vent fields at EPR-9°50'N and SEPR. Convection within the lower crust magma chamber could also explain the formation of high-heat flux vent fields as crystallization of this melt delivered by magmatic convection cells at the top of magmatic upflows releases $\sim$100–200 MW right beneath vent fields. Additional heat could come from the cooling of the upper basaltic crust on 5–10 kms both along and across-axis.

Our hypothesis that the lower crust is convecting challenges classical views of MOR lower crust accretion being "passive." It provides a mechanism for melt transport from moho level to the AML. Melt contained in magmatic upflows would be delivered to AML sections every 8–10 kms, as suggested for melt-rich sections along the EPR-9°50'N AML. The thermal convection model predicts pronounced along-axis variability of melt differentiation and crustal accretion processes. In and next to zones of magmatic upflows, the model is compatible with a strong contribution of "gabbro-glacier" model-type crustal accretion in which the lower crust crystallized in the AML from melt coming from moho level flows in a ductile way across-axis. It also introduces the notion that lower crustal accretion at fast-spreading ridges may occur in two stages: one stage in the convecting near-axis corridor followed by passive accretion, and further crystallization and melt-crystal reaction in each diverging plate.

Our model relies on the key assumption that melt segregation and associated compaction processes in the lower gabbroic mush organize themselves so that local melt enrichment leads to a decrease of the effective viscosity of the gabbros favoring the onset of thermal convective instabilities. Future work should be devoted in the community to further testing these ideas using numerical models coupling mush convection to melt segregation. These will help constraining the dynamics of melt delivery from the mantle and how it critically controls the stability of the convective process, by preserving (or not) the integrity of the convective loops preventing them from melt "dryout." Finally, the understanding of the dynamics of these magmatic-hydrothermal couplings between the upper and lower crust would also benefit from a three-dimensional study coupling along-axis convection and cross-axis crustal accretion to hydrothermal convection.

## References

Allwright, J., and R. F. Katz (2014), Pipe Poiseuille flow of viscously anisotropic, partially molten rock, *Geophys. J. Int.*, *199*(3), 1608–1624.
Anderko, A., and K. S. Pitzer (1993), Equation-of-state representation of phase equilibria and volumetric properties of the system NaCl-H$_2$O above 573K, *Geochim. Cosmochim. Acta*, *57*, 1657–1680.

Benn, K., A. Nicolas, and I. Reuber (1988), Mantle-crust transition zone and origin of wehrlitic magmas: Evidence from the Oman ophiolite, *Tectonophysics*, *151*(1), 75–85.

Bercovici, D., Y. Ricard, and G. Schubert (2001), A two-phase model for compaction and damage: 1. General theory, *J. Geophys. Res.*, *106*(B5), 8887–8906.

Bottinga, Y., and D. F. Weill (1972), The viscosity of magmatic silicate liquids; a model calculation, *Am. J. Sci.*, *272*(5), 438–475.

Boudier, F., A. Nicolas, and B. Ildefonse (1996), Magma chambers in the Oman ophiolite: Fed from the top and the bottom, *Earth Planet. Sci. Lett.*, *144*(1), 239–250.

Brandeis, G., and C. Jaupart (1986), On the interaction between convection and crystallization in cooling magma chambers, *Earth Planet. Sci. Lett.*, *77*(3), 345–361.

Buck, W. R. (2000), Can downward flow of dense cumulate slurry through mushy upper gabbros produce lower gabbros at a fast-spreading center?, *Geol. Soc. Am. Spec. Pap.*, *349*, 121–128.

Canales, J. P., M. R. Nedimović, G. M. Kent, S. M. Carbotte, and R. S. Detrick (2009), Seismic reflection images of a near-axis melt sill within the lower crust at the Juan de Fuca ridge, *Nature*, *460*(7251), 89–93.

Cannat, M., J. Cann, and J. Maclennan (2004), Some hard rock constraints on the supply of heat to mid-ocean ridges, in *Mid-Ocean Ridges*, edited by C. R. German, J. Lin, and L. M. Parson, pp. 111–149, AGU, Washington, D. C., doi:10.1029/148GM05.

Carbotte, S. M., M. Marjanović, H. Carton, J. C. Mutter, J. P. Canales, M. R. Nedimović, S. Han, and M. R. Perfit (2013), Fine-scale segmentation of the crustal magma reservoir beneath the East Pacific Rise, *Nat. Geosci.*, *6*(10), 866–870.

Ceuleneer, G., and M. Rabinowicz (1993), Mantle flow and melt migration beneath oceanic ridges: Models derived from observations in ophiolites, in *Mantle Flow and Melt Generation at Mid-Ocean Ridges*, edited by J. P. Morgan, D. K. Blackman, and J. M. Sinton, pp. 123–154, AGU, Washington, D. C., doi:10.1029/GM071p0123.

Chenevez, J., P. Machetel, and A. Nicolas (1998), Numerical models of magma chambers in the Oman ophiolite, *J. Geophys. Res.*, *103*(B7), 15,443–15,455.

Cherkaoui, A. S., and W. S. Wilcock (1999), Characteristics of high Rayleigh number two-dimensional convection in an open-top porous layer heated from below, *J. Fluid Mech.*, *394*, 241–260.

Cherkaoui, A. S., W. S. Wilcock, R. A. Dunn, and D. R. Toomey (2003), A numerical model of hydrothermal cooling and crustal accretion at a fast spreading mid-ocean ridge, *Geochem. Geophys. Geosyst.*, *4*(9), 8616, doi:10.1029/2001GC000215.

Coogan, L. A. (2014), *The Lower Oceanic Crust, in «The Crust»*, pp. 497–541, Elsevier, Amsterdam, doi:10.1016/B978-0-08-095975-7.00316-8.

Coogan, L. A., K. M. Gillis, C. J. MacLeod, G. M. Thompson, and R. Hékinian (2002), Petrology and geochemistry of the lower ocean crust formed at the East Pacific Rise and exposed at Hess Deep: A synthesis and new results, *Geochem. Geophys. Geosyst.*, *3*(11), 8604, doi: 10.1029/2001GC000230.

Conte, S. D., and R. T. Dames (1958), An alternating direction method for solving the biharmonic equation, *Math. Tables Other Aids Comput.*, *12*(63), 198–205.

Coumou, D., T. Driesner, S. Geiger, C. A. Heinrich, and S. Matthäi (2006), The dynamics of mid-ocean ridge hydrothermal systems: Splitting plumes and fluctuating vent temperatures, *Earth Planet. Sci. Lett.*, *245*(1), 218–231.

Coumou, D., T. Driesner, and C. A. Heinrich (2008), The structure and dynamics of mid-ocean ridge hydrothermal systems, *Science*, *321*, 1825–1828.

Crawford, W. C., S. C. Webb, and J. A. Hildebrand (1999), Constraints on melt in the lower crust and Moho at the East Pacific Rise, 9 48′ N, using seafloor compliance measurements, *J. Geophys. Res.*, *104*(B2), 2923–2939.

Danyushevsky, L. V., and P. Plechov (2011), Petrolog3: Integrated software for modeling crystallization processes, *Geochem. Geophys. Geosyst.*, *12*, Q07021, doi:10.1029/2011GC003516.

Detrick, R. S., P. Buhl, E. Vera, J. Mutter, J. Orcutt, J. Madsen, and T. Brocher (1987), Multi-channel seismic imaging of a crustal magma chamber along the East Pacific Rise, *Nature*, *326*(6108), 35–41.

Detrick, R. S., A. J. Harding, G. M. Kent, J. A. Orcutt, J. C. Mutter, and P. Buhl (1993), Seismic structure of the southern East Pacific Rise, *Science*, *259*(5094), 499–503.

Douglas, J., and H. H. Rachford (1956), On the numerical solution of heat conduction problems in two and three space variables, *Trans. Am. Math. Soc.*, *82*(2), 421–439.

Dunn, R. A., D. R. Toomey, and S. C. Solomon (2000), Three-dimensional seismic structure and physical properties of the crust and shallow mantle beneath the East Pacific Rise at 9° 30′N, *J. Geophys. Res.*, *105*(B10), 23,537–23,555.

Fontaine, F. J., and W. S. Wilcock (2007), Two-dimensional numerical models of open-top hydrothermal convection at high Rayleigh and Nusselt numbers: Implications for mid-ocean ridge hydrothermal circulation, *Geochem. Geophys. Geosyst.*, *8*, Q07010, doi:10.1029/2007GC001601.

Fontaine, F. J., J. A. Olive, M. Cannat, J. Escartin, and T. Perol (2011), Hydrothermally-induced melt lens cooling and segmentation along the axis of fast-and intermediate-spreading centers, *Geophys. Res. Lett.*, *38*, L14307, doi:10.1029/2011GL047798.

Fornari, D. J., R. M. Haymon, M. R. Perfit, T. K. Gregg, and M. H. Edwards (1998), Axial summit trough of the East Pacific Rice 9°–10° N: Geological characteristics and evolution of the axial zone on fast spreading mid-ocean ridge, *J. Geophys. Res.*, *103*(B5), 9827–9855.

Geiger, S., T. Driesner, C. A. Heinrich, and S. K. Matthäi (2005), On the dynamics of NaCl-H$_2$O fluid convection in the Earth's crust, *J. Geophys. Res.*, *110*, doi:10.1029/2004JB003362.

Garmany, J. (1989), Accumulations of melt at the base of young oceanic crust, *Nature*, *340*, 628–632.

Gillis, K. M., et al. (2014). Primitive layered gabbros from fast-spreading lower oceanic crust, *Nature*, *505*(7482), 204–207.

Hasenclever, J., S. Theissen-Krah, L. H. Rüpke, J. P. Morgan, K. Iyer, S. Petersen, and C. W. Devey (2014), Hybrid shallow on-axis and deep off-axis hydrothermal circulation at fast-spreading ridges, *Nature*, *508*(7497), 508–512.

Hirth, G., J. Escartin, and J. Lin (1998), The rheology of the lower oceanic crust: Implications for lithospheric deformation at mid-ocean ridges, in *Faulting and Magmatism at Mid-Ocean Ridges*, edited by W. Roger Buck et al., AGU, Washington, D. C., doi:10.1029/GM106p0291.

Iturrino, G. J., D. J. Miller, and N. I. Christensen (1996), Velocity behavior of lower crustal and upper mantle rocks from a fast-spreading ridge at Hess-Deep, in *Proc. Ocean Drill. Program Sci. Results*, *147*, 417–440.

Johnson, H. P., M. A. Tivey, T. A. Bjorklund, and M. S. Salmi (2010), Hydrothermal circulation within the Endeavour segment, Juan de Fuca Ridge, *Geochem. Geophys. Geosyst.*, *11*, Q05002, doi:10.1029/2009GC002957.

Jupp, T., and A. Schultz (2000), A thermodynamic explanation for black smoker temperatures, *Nature*, *403*, 880–883.

Katz, R. F., and Y. Takei (2013), Consequences of viscous anisotropy in a deforming, two-phase aggregate: Part 2. Numerical solutions of the full equations, *J. Fluid Mech.*, *734*, 456–485.

Kelemen, P. B., K. Koga, and N. Shimizu (1997), Geochemistry of gabbro sills in the crust-mantle transition zone of the Oman ophiolite: Implications for the origin of the oceanic lower crust, *Earth Planet. Sci. Lett.*, *146*(3), 475–488.

Kellog, J. (2011), Temporal and spatial variability of hydrothermal fluxes within a mid-ocean ridge segment, PhD thesis, Univ. of Washington, Seattle.

Korenaga, J., and P. B. Kelemen (1997), Origin of gabbro sills in the Moho transition zone of the Oman ophiolite: Implications for magma transport in the oceanic lower crust, *J. Geophys. Res.*, *102*(B12), 27,729–27,749.

Lejeune, A. M., and P. Richet (1995), Rheology of crystal-bearing silicate melts: An experimental study at high viscosities, *J. Geophys. Res.*, *100*(B3), 4215–4229.

Lowell, R. P., A. Farough, J. Hoover, and K. Cummings (2013), Characteristics of magma-driven hydrothermal systems at oceanic spreading centers, *Geochem. Geophys. Geosyst.*, *14*, 1756–1770, doi:10.1002/ggge.20109.

Maclennan, J., T. Hulme, and S. C. Singh (2004), Thermal models of oceanic crustal accretion: Linking geophysical, geological and petrological observations, *Geochem. Geophys. Geosyst.*, *5*, Q02F25, doi:10.1029/2003GC000605.

Marjanović, M., S. M. Carbotte, H. Carton, M. R. Nedimović, J. C. Mutter, and J. P. Canales (2014), A multi-sill magma plumbing system beneath the axis of the East Pacific Rise, *Nat. Geosci.*, *7*(11), 825–829.

McKenzie, D. P., J. M. Roberts, and N. O. Weiss (1974), Convection in the Earth's mantle: Towards a numerical simulation, *J. Fluid Mech.*, *62*(3), 465–538.

Menand, T., K. A. Daniels, and P. Benghiat (2010), Dyke propagation and sill formation in a compressive tectonic environment, *J. Geophys. Res.*, *115*, B08201, doi:10.1029/2009JB006791.

Meyer, C. A., R. B. McClintock, G. J. Silvestri, and R. C. Spencer (1993), ASME Steam Tables: Thermodynamic and Transport Properties of Steam, 436 pp., Am. Soc. of Mech. Eng., New York.

Morgan, J. P., and Y. J. Chen (1993), The genesis of oceanic crust: Magma injection, hydrothermal circulation, and crustal flow, *J. Geophys. Res.*, *98*(B4), 6283–6297.

Mottl, M. J. (2003), Partitioning of energy and mass fluxes between mid-ocean ridge axes and flanks at high and low temperature, in *Energy and Mass Transfer in Marine Hydrothermal Systems*, edited by P. E. Halbach et al., pp. 271–286, Dahlem Univ. Press, Berlin.

Nedimović, M. R., S. M. Carbotte, A. J. Harding, R. S. Detrick, J. P. Canales, J. B. Diebold, G. M. Kent, M. Tischer and J. M. Babcock (2005), Frozen magma lenses below the oceanic crust, *Nature*, *436*(7054), 1149–1152.

Nicolas, A., and B. Ildefonse (1996), Flow mechanism and viscosity in basaltic magma chambers, *Geophys. Res. Lett.*, *23*(16), 2013–2016.

Parmentier, E. M. (1978), A study of thermal convection in non-Newtonian fluids, *J. Fluid Mech.*, *84*, 1–11.

Parmentier, E. M., D. L. Turcotte, and K. E. Torrance (1976), Studies of finite-amplitude non-Newtonian thermal convection with application to convection in the earth's mantle, *J. Geophys. Res.*, *81*(11), 1839–1846.

Perk, N. W., L. A. Coogan, J. A. Karson, E. M. Klein, and H. D. Hanna (2007), Petrology and geochemistry of primitive lower oceanic crust from Pito Deep: Implications for the accretion of the lower crust at the Southern East Pacific Rise, *Contrib. Mineral. Petrol.*, *154*(5), 575–590.

Petitjean, S., M. Rabinowicz, M. Grégoire, and S. Chevrot (2006), Differences between Archean and Proterozoic lithospheres: Assessment of the possible major role of thermal conductivity, *Geochem. Geophys. Geosyst.*, *7*, Q03021, doi:10.1029/2005GC001053.

Picard, D., L. Arbaret, M. Pichavant, R. Champallier, and P. Launeau (2013), The rheological transition in plagioclase-bearing magmas, *J. Geophys. Res. Solid Earth*, *118*, 1363–1377, doi:10.1002/jgrb.50091.

Pitzer, K. S., J. C. Peiper, and R. H. Busey (1984), Thermodynamic properties of aqueous sodium chloride solutions, *J. Phys. Chem. Ref Data*, *13*, 1–106.

Rabinowicz, M., and J. L. Vigneresse (2004), Melt segregation under compaction and shear channeling: Application to granitic magma segregation in a continental crust, *J. Geophys. Res.*, *109*, B04407, doi:10.1029/2002JB002372.

Rabinowicz, M., G. Ceuleneer, and A. Nicolas (1987), Melt segregation and flow in mantle diapirs below spreading centers: Evidence from the Oman ophiolite, *J. Geophys. Res.*, *92*(B5), 3475–3486.

Rabinowicz, M., P. Genthon, G. Ceuleneer, and M. Hillairet (2001), Compaction in a mantle mush with high melt concentrations and the generation of magma chambers, *Earth Planet. Sci. Lett.*, *188*(3), 313–328.

Rabinowicz, M., M. Bystricky, M. Schmocker, M. J. Toplis, A. Rigo, and H. Perfettini (2010), Development of fluid veins during deformation of fluid-rich rocks close to the brittle–ductile transition: Comparison between experimental and physical models, *J. Petrol.*, *51*(10), 2047–2066.

Richter, F. M., and S. F. Daly (1978), Convection models having a multiplicity of large horizontal scales, *J. Geophys. Res.*, *83*(B10), 4951–4956.

Rubin, A. M., and D. D. Pollard (1988), Dike-induced faulting in rift zones of Iceland and Afar, *Geology*, *16*(5), 413–417.

Rubin, K., and J. Sinton (2007), Inferences on mid-ocean ridge thermal and magmatic structure from MORB compositions, *Earth. Planet. Sci. Lett.*, *260*, 257–276.

Singh, S. C., G. M. Kent, J. S. Collier, A. J. Harding, and J. A. Orcutt (1998), Melt to mush variations in crustal magma properties along the ridge crest at the southern East Pacific Rise, *Nature*, *394*(6696), 874–878.

Singh, S. C., et al. (2006), Seismic reflection images of the Moho underlying melt sills at the East Pacific Rise, *Nature*, *442*(7100), 287–290.

Sinton, J. M., and R. S. Detrick (1992), Mid-ocean ridge magma chambers, *J. Geophys. Res.*, *97*(B1), 197–216.

Takei, Y., & R. F. Katz (2013), Consequences of viscous anisotropy in a deforming, two-phase aggregate. Part 1. Governing equations and linearized analysis, *J. Fluid Mech.*, *734*, 424–455.

Theissen-Krah, S., K. Iyer, L. H. Rüpke, and J. P. Morgan (2011), Coupled mechanical and hydrothermal modeling of crustal accretion at intermediate to fast spreading ridges, *Earth Planet. Sci. Lett.*, *311*(3), 275–286.

Theissen-Krah, S., L. H. Rüpke, and J. Hasenclever (2016), Modes of crustal accretion and their implications for hydrothermal circulation, *Geophys. Res. Lett.*, *43*, 1124–1131, doi:10.1002/2015GL067335.

Von Damm, K. L. (2004), Evolution of the hydrothermal system at East Pacific Rise 9°50′N: Geochemical evidence for changes in the upper oceanic crust, in *Mid-Ocean Ridges*, edited by C. R. German, J. Lin and L. M. Parson, American Geophysical Union, Washington, D. C., doi:10.1029/148GM12.

Wilcock, W. S., E. E. Hooft, D. R. Toomey, P. R. McGill, A. H. Barclay, D. S. Stakes, and T. M. Ramirez (2009), The role of magma injection in localizing black-smoker activity, *Nat. Geosci.*, *2*(7), 509–513.

Wilson, D. S, S. A. Clague, N. H. Sleep, and J. L. Morton (1988), Implication of magma convection for the size and temperature of magma chambers at fast spreading ridges, *J. Geophys. Res.*, *93*(B10), 11,974–11,984.

Wood, J. R., and T. A. Hewett (1982), Fluid convection and mass transfer in porous sandstones: A theoretical model, *Geochim. Cosmochim. Acta*, *46*, 1707–1713.

Xu, M., J. Pablo Canales, S. M. Carbotte, H. Carton, M. R. Nedimović, and J. C. Mutter (2014), Variations in axial magma lens properties along the East Pacific Rise (9° 30′ N–10° 00′ N) from swath 3-D seismic imaging and 1-D waveform inversion, *J. Geophys. Res. Solid Earth*, *119*, 2721–2744, doi:10.1002/2013JB010730.

Yoshinobu, A. S., and G. Hirth (2002), Microstructural and experimental constraints on the rheology of partially molten gabbro beneath oceanic spreading centers, *J. Struct. Geol.*, *24*(6), 1101–1107.